

ABSTRACT

RICHARDSON, ANDREW CONNOR. Comparison of Heat Transfer Enhancement Features in a Four-Passage Serpentine Cooling Design. (Under the direction of Dr. Srinath Ekkad).

Gas turbine airfoil blades often feature internal cooling channels connected via 180 degree bends. The effects of the Coriolis force results in a situation in which there is increased heat transfer on the trailing side and decreased heat transfer on the leading side for radially outward flows. This scenario leads to nonuniform blade temperatures and increased thermal stresses, which are detrimental to overall blade lifespan. This study presents two novel configurations of ribbed turbulators for a four-passage geometry of serpentine channels: The V-Ribbed and Broken V-Ribbed configurations. Heat transfer simulations were carried out for Reynolds numbers ranging from 18933 to 80524 under stationary conditions, and for a Reynolds number of 18933 with a non-dimensional rotation number of 0.11 under rotating conditions. The conditions under which these simulations were run represent those of the test setup for the experimental case, in which the conductive heat transfer from the walls of the test section is ignored. This study focuses on the convective heat transfer happening within the channel. Frictional losses caused by the 180 degree bends in the serpentine geometry were evaluated in terms of normalized friction factor and pumping power. The configurations explored were ranked based on their thermal hydraulic performances. Heat transfer enhancement levels under rotating conditions were largely consistent with, if not slightly higher than, those under stationary conditions, with some exceptions due to the lasting effects of the radially outward inlet passage. The Broken V-Ribbed configuration was found to produce the highest levels of heat transfer.

© Copyright 2021 by Andrew Connor Richardson

All Rights Reserved

Comparison of Heat Transfer Enhancement Features in a Four-Passage Serpentine Cooling
Design

by
Andrew Connor Richardson

A thesis submitted to the Graduate Faculty of
North Carolina State University
in partial fulfillment of the
requirements for the degree of
Master of Science

Aerospace Engineering

Raleigh, North Carolina
2021

APPROVED BY:

Srinath Ekkad
Committee Chair

Tarek Echehki

Richard Gould

DEDICATION

This paper is dedicated to my loving parents, whose unwavering support kept me focused on completing my goal.

BIOGRAPHY

Andrew Richardson was born in Atlanta, Georgia. After completing his high school education at George Walton Comprehensive High School in Marietta, Georgia in 2014, Andrew attended Clemson University to study engineering. Between the years of 2017 and 2018, he participated in a cooperative education program with Techtronic Industries. Following his graduation in 2019 with a Bachelor of Science in Mechanical Engineering, Andrew entered the Mechanical and Aerospace Engineering graduate program at North Carolina State University to pursue his master's degree.

TABLE OF CONTENTS

LIST OF TABLES	v
LIST OF FIGURES	vi
LIST OF SCHEMES, SYMBOLS, OR TERMINOLOGY	viii
Chapter 1: Numerical Setup	1
Introduction.....	1
Test Section.....	2
Meshing and Grid Independence	6
Solver and Turbulence Model.....	7
Boundary Conditions	7
Heat Transfer Coefficient Calculation	8
Chapter 2: Results and Discussion	9
Detailed Nusselt Number Ratio Under Stationary and Rotating Conditions.....	9
Smooth Channel Configuration Under Stationary Conditions	9
Smooth Channel Configuration Under Rotating Conditions	11
V-Ribbed Channel Configuration Under Stationary Conditions	13
V-Ribbed Channel Configuration Under Rotating Conditions.....	15
Broken V-Ribbed Channel Configuration Under Stationary Conditions	17
Broken V-Ribbed Channel Configuration Under Rotating Conditions.....	18
Passagewise-Averaged Nusselt Number Ratio Under Stationary and Rotating Conditions	19
Frictional Factor, Overall Nusselt Number Ratio, and Thermal Hydraulic Performance	23
Conclusion	25
References	26

LIST OF TABLES

Table 1.1	Important dimensions and design constraints.	5
-----------	---	---

LIST OF FIGURES

Figure 1.1:	Orientation of serpentine passages in reference to gas turbine airfoils.....	1
Figure 1.2:	Cooling configuration geometrical details for (a) the Smooth channel and V-Ribbed channel configurations, and (b) the Broken V-Ribbed channel configuration.	3
Figure 1.3:	Different views of the grid used for computations: (a) the orthogonal plane and (b) the bend region.....	6
Figure 2.1:	Detailed Nusselt number ratio contour for the Smooth channel configuration under stationary and rotating conditions.	10
Figure 2.2:	Smooth channel velocity vector flow fields with normalized fluid temperature contour at planes orthogonal to bulk coolant flow (under stationary conditions, $Re = 18933$, $Ro = 0$).	11
Figure 2.3:	Smooth channel velocity vector flow fields with normalized fluid temperature contour at planes orthogonal to bulk coolant flow (under rotating conditions, $Re = 18933$, $Ro = 0.11$).	13
Figure 2.4:	Detailed Nusselt number ratio contour for the V-Ribbed channel configuration under stationary and rotating conditions.....	14
Figure 2.5:	V-Ribbed channel velocity vector flow fields with normalized fluid temperature contour at planes orthogonal to bulk coolant flow (under stationary conditions, $Re = 18933$, $Ro = 0$).....	15
Figure 2.6:	V-Ribbed channel velocity vector flow fields with normalized fluid temperature contour at planes orthogonal to bulk coolant flow (under rotating conditions, $Re = 18933$, $Ro = 0.11$).	16
Figure 2.7:	Detailed Nusselt number ratio contour for the Broken V-Ribbed channel configuration under stationary and rotating conditions.....	17
Figure 2.8:	Broken V-Ribbed channel velocity vector flow fields with normalized fluid temperature contour at planes orthogonal to bulk coolant flow (under stationary conditions, $Re = 18933$, $Ro = 0$).....	18
Figure 2.9:	Broken V-Ribbed channel velocity vector flow fields with normalized fluid temperature contour at planes orthogonal to bulk coolant flow (under rotating conditions, $Re = 18933$, $Ro = 0.11$).	19

Figure 2.10: Passagewise-averaged Nusselt number ratio under stationary and rotating conditions for (a) V-Ribbed and Smooth channel configurations and (b) Broken V-Ribbed and Smooth channel configurations.....	21
Figure 2.11: Normalized friction factor and pumping power variation with Reynolds number.....	23
Figure 2.12: Globally averaged Nusselt number ratio (Nu/Nu_0) and thermal hydraulic performance variation with Reynolds number.....	25

LIST OF SCHEMES, SYMBOLS, OR TERMINOLOGY

Nomenclature

Gr = Grashof number

g = acceleration due to gravity (m/s^2)

β = coefficient of thermal expansion ($1/\text{K}$)

h = heat transfer coefficient ($\text{W/m}^2 \text{K}$)

q'' = heat flux (W/m^2)

T_w = wall temperature (K)

T_m = mainstream temperature (K)

Nu = Nusselt number

Nu_0 = Dittus-Boelter correlation, $0.023\text{Re}^{0.8}\text{Pr}^{0.4}$

d_h = channel hydraulic diameter (m)

k_f = thermal conductivity of air (W/m K)

Re = Reynolds number, Vd_h/ν

Pr = Prandtl number, ν/α

f = friction factor

Δp = pressure drop (Pascal)

V = average coolant velocity (m/s)

L_{total} = total length of serpentine passage (m)

Ro = rotation number, $\Omega d_h/V$

P = pumping power (W)

\dot{V} = volumetric air flow rate (m^3/s)

Greek Symbols

ρ = density (kg/m^3)

ν = kinematic viscosity (m^2/s)

α = thermal diffusivity (m^2/s)

Ω = rotation speed (rpm)

Abbreviations

THP = thermal hydraulic performance

CHAPTER 1: Numerical Setup

Introduction

Modern gas turbine airfoils are equipped with internal and external cooling features, such as jet impingement, serpentine passages, and film cooling. This study explores the addition of heat transfer enhancement features to the serpentine passages, in the form of turbulence promoters. The context of these serpentine passages is shown in Figure 1.1. The presence of ribbed turbulators increases the near-wall stress and generates additional secondary flows. These secondary flows interact with the serpentine geometry to create large-scale vortices which act to enhance the turbulent transport, in turn improving the overall heat transfer in the channel.

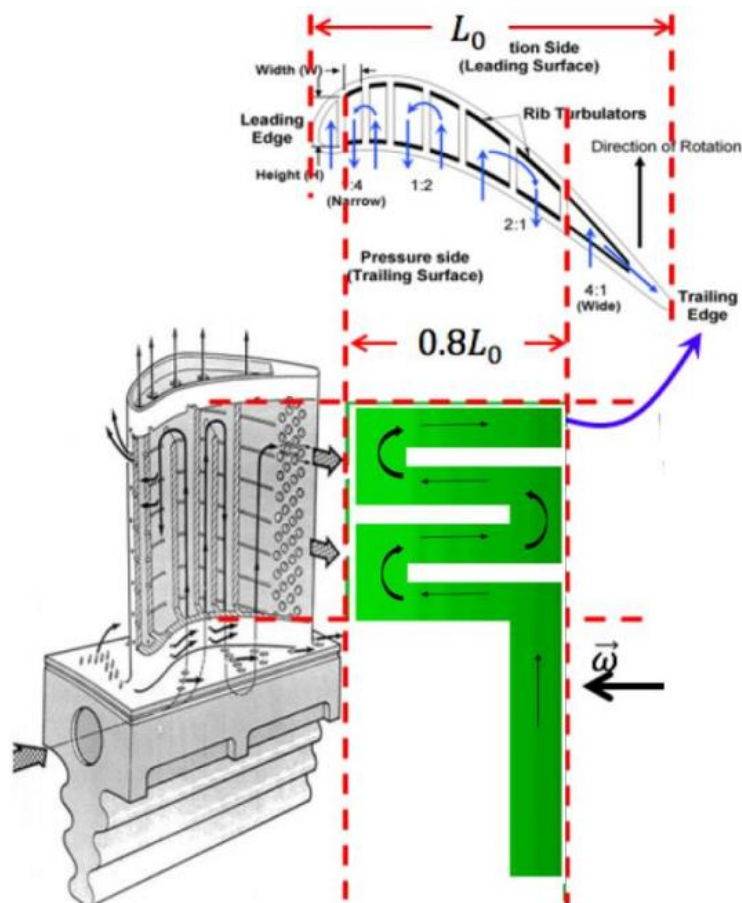
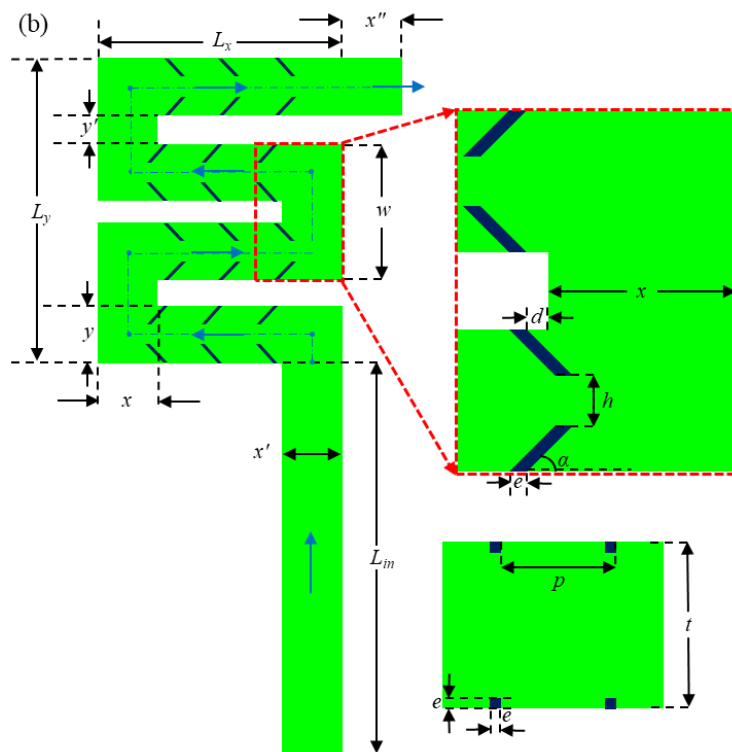
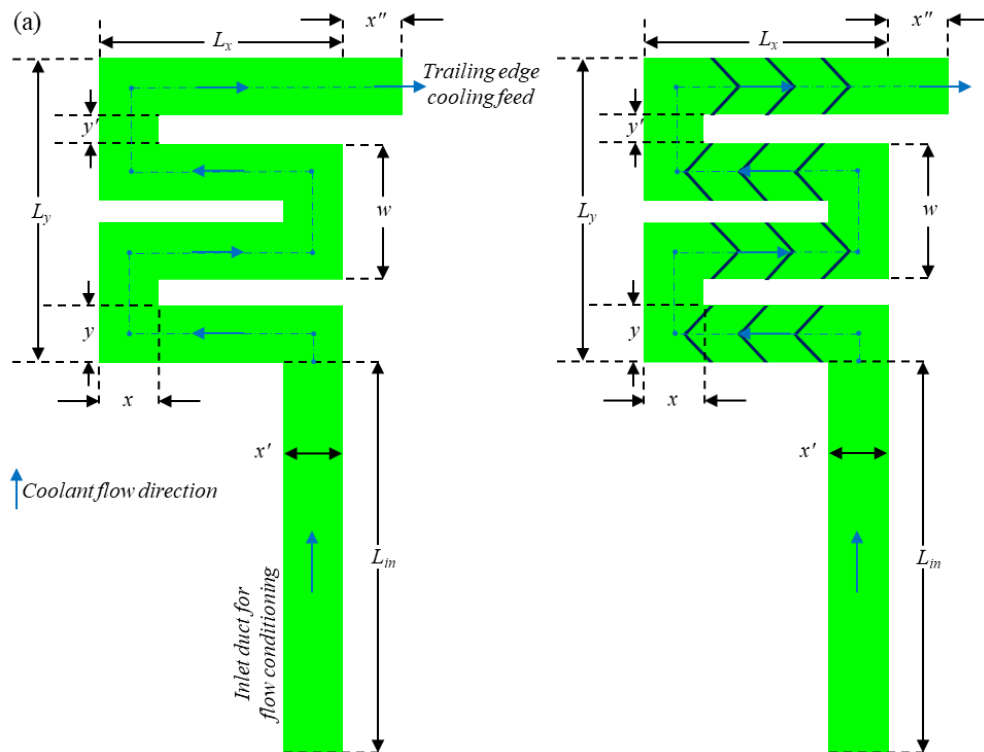


Figure 1.1: Orientation of serpentine passages in reference to gas turbine airfoils.

Test Section

The serpentine geometry investigated in this study has been explored previously in other rotational heat transfer studies, the details of which can be found in Reference [1]. This study added two separate heat transfer enhancement features in the form of ribbed turbulators on the leading and trailing sides of the horizontal passages. The layout of the three geometries is outlined below in Figure 1.2.

Figure 1.2: Cooling configuration geometrical details for (a) the Smooth channel and V-Ribbed channel configurations, and (b) the Broken V-Ribbed channel configuration.



The ribbed turbulator designs were chosen to maximize heat transfer enhancement within the rectangular passages via the production of additional secondary flows and higher local wall turbulence. The inspiration for these designs was found in Reference [2]. The detailed geometrical parameters, relationships, and constraints are listed in Table 1.1.

Table 1.1: Important dimensions and design constraints.

	Four-passage dimensions (mm)	Relationships/Constraints
d_h	24.00	$2yt / (y + t)$
L_{in}	165.10	$1.625L_x = 1.3L_0$
L_x	101.60	$0.8L_0$
L_y	127.00	$L_0 = ny + n'y'$
x	24.00	d_h
x'	25.40	-
x''	25.40	-
y	22.75	$(0.2L_0 / n) \left[-(n-3) + \sqrt{n^2 - n + 9} \right]$
y'	12.00	$0.5d_h = yt / (y + t)$
t	25.40	$0.2L_0$
w	57.49	$2y + y'$
α	45°	-
d	0.96	-
e	2.38	$e = 0.1p = 0.1d_h$

Table 1.1 (continued).

p	23.8	$p/e = 10, p = d_h$
h	5.00	-

Meshing and Grid Independence

A 10.5 million element mesh of the test section geometry was generated using ANSYS. The mesh used inflation layers with a first layer thickness of 1e-4 m and a wall $y+$ of around 5. A grid independence study was carried out with meshes ranging from 7.5 million to 15 million elements, yielding results indicating that the level of mesh detail did not impact the results of the simulations. Portions of the grid are shown in Figure 1.3 below.

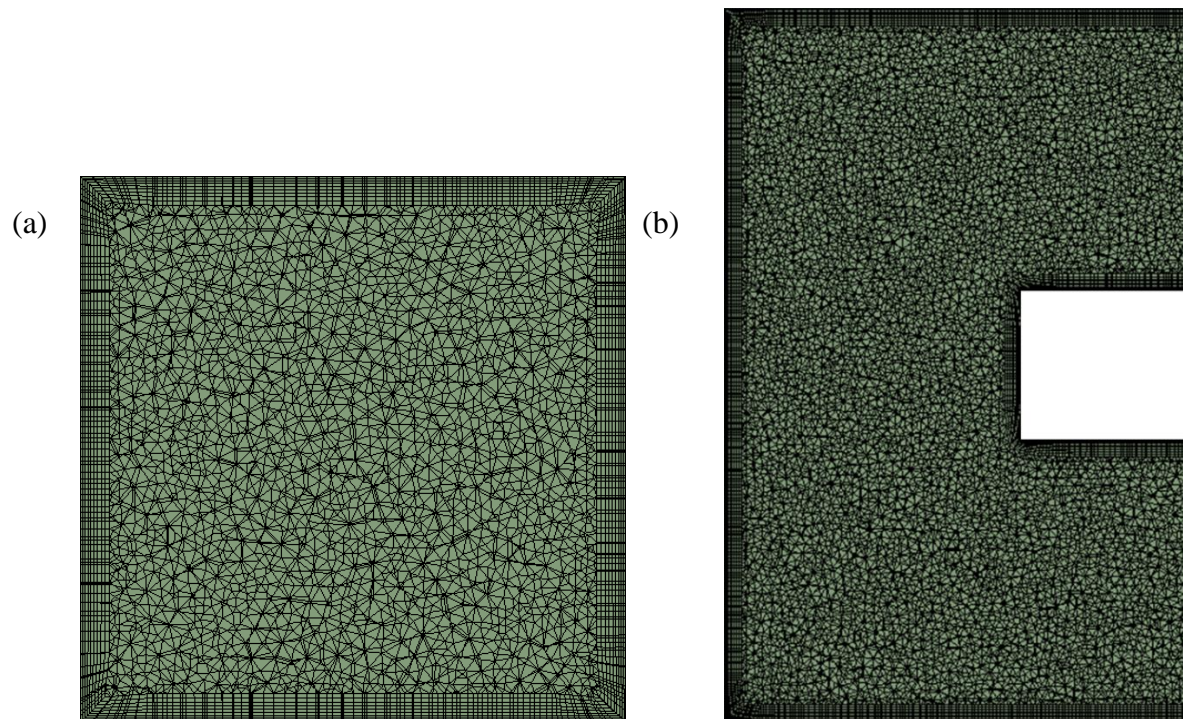


Figure 1.3: Different views of the grid used for computations: (a) the orthogonal plane and (b) the bend region.

Solver and Turbulence Model

A series of fluid flow simulations was performed using ANSYS Fluent. The calculations were carried at a range of Reynolds numbers from 18933 to 80524 for the stationary case and a Reynolds number of 18933 for the rotating case. For the rotating case, a Rotation number of 0.11 was employed. A pressure-based solver was used as the working fluid was assumed to be incompressible. The Semi-Implicit Method for Pressure-Linked Equations scheme was used for the pressure-velocity coupling. A realizable k - ϵ turbulence model with enhanced wall treatment was used.

Boundary Conditions

The mass flowrate at the inlet was determined based off the operating Reynolds number and channel hydraulic diameter. A uniform heat flux of 5000 W/m^2 was applied to the leading and trailing walls of the geometry. The remaining inner and outer walls were adiabatic. The temperature at the inlet was set at 300 K. The turbulence intensity and turbulent length scale at the inlet were set at 5% and equal to the hydraulic diameter, respectively. Zero gauge pressure was specified at the outlet. The solution was assumed to be converged when the continuity and energy residuals reached 10^{-6} and 10^{-8} , respectively. The Richardson number was calculated to be 2.36×10^{-4} for the case with the maximum temperature difference, meaning that the effects of natural convection were negligible. As such, the impact of the centrifugal buoyancy force was found to be insignificant. The Richardson number was found using the ratio of the Grashof number to the square of the Reynolds number. The formula for the Grashof number is shown below:

$$\text{Gr} = \frac{g\beta(T_w - T_m)d_h^3}{\nu^2} \quad (1.1)$$

Heat Transfer Coefficient Calculation

The local heat transfer coefficient at the walls subjected to constant heat flux was calculated using the following equation:

$$h(x, y) = \frac{q''}{T_w(x, y) - T_m(x)} \quad (1.2)$$

The local bulk fluid temperature was calculated by linearly interpolating the obtained bulk fluid temperature data in the streamwise direction. The Nusselt number ratio, or normalized Nusselt number, was then calculated using the equation below:

$$\frac{\text{Nu}(x, y)}{\text{Nu}_0} = \frac{h(x, y)d_h}{k_f(0.023\text{Re}^{0.8}\text{Pr}^{0.4})} \quad (1.3)$$

The Nu_0 value was derived from the Dittus-Boelter correlation for turbulent flow through a rectangular channel.

CHAPTER 2: Results and Discussion

Detailed Nusselt Number Ratio Under Stationary and Rotating Conditions

Detailed heat transfer coefficient measurements were recorded and analyzed under stationary and rotating conditions. The tests were run under the condition that there was no conduction from the walls. The rotating cases were conducted at a non-dimensionalized Rotation number of 0.11. Passagewise-averaged normalized Nusselt numbers (Nu/Nu_0) at the wall surface were calculated and are presented in the figures below. Of the three configurations analyzed, only one did not feature any heat transfer enhancement features in order to act as the control case and is referred to as the “smooth channel.” The remaining configurations contained heat transfer enhancement features in the form of V-shaped ribs and V-shaped ribs that do not meet in the middle. The former is referred to as the “V-Ribbed” configuration, while the latter is referred to as the “Broken V-Ribbed” configuration. These configurations were designed with the goal of generating the largest heat transfer levels via a combination of rib-induced secondary flows and Dean-type vortices created by the 180 degree bends in the geometry.

Smooth Channel Configuration Under Stationary Conditions

The normalized Nusselt number contours under both stationary and rotating conditions is shown in Figure 2.1. It should be noted that this figure displays the Nusselt number ratios at the wall surface. As the coolant enters the first passage, a large part of it impinges upwards on the inner horizontal wall, while a smaller part turns along the outer horizontal wall due to low flow resistance. This fluid motion results in enhanced heat transfer at both locations in the first passage.

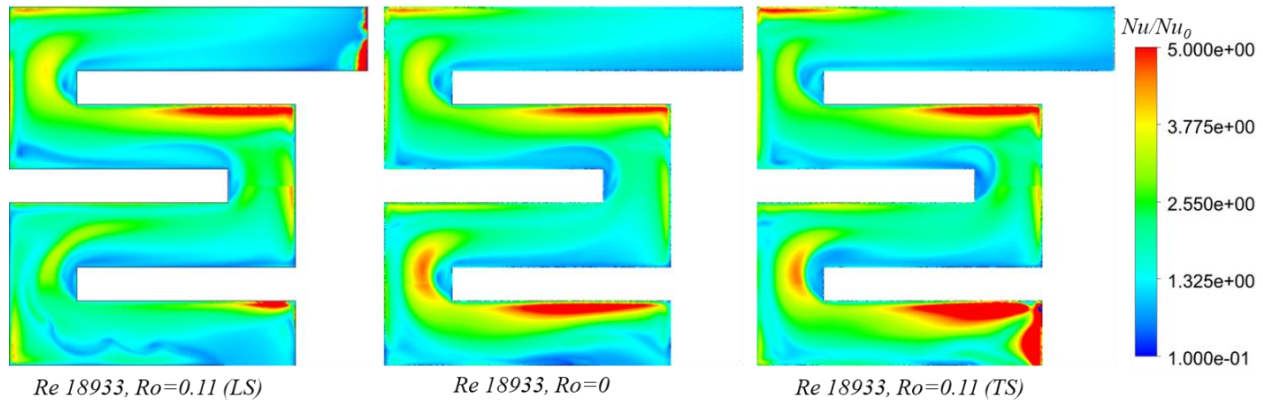


Figure 2.1: Detailed Nusselt number ratio contour for the Smooth channel configuration under stationary and rotating conditions.

As the fluid flows through the 180 degree bends in the channel, elevated levels of heat transfer enhancement are seen due to fluid acceleration and deceleration from radial pressure gradient and inertial effects. Specifically, elevated levels of heat transfer enhancement are seen along the outer vertical walls and on the outer top vertical corners. In addition, counter-rotating pairs of vortices, known as Dean-type vortices, are formed within the channel after passing through the inlet into the first passage. An example of a pair of Dean-type vortices is shown in P_1 in Figure 2.2. This phenomenon results in the enhancement of turbulent transport of energy between the top and bottom walls. The exchanged heat energy from the walls is brought to the center of the channel, while the relatively cooler fluid is directed towards the outer walls. This further mixing yields improved heat exchange of the coolant.

While the distribution of heat transfer enhancement in the first passage was predominately affected by the inlet conditions, the second and third passages experienced different distributions of heat transfer enhancement. In these passages, the primary source of heat transfer enhancement was a combination of local fluid acceleration, increased turbulent transport due to the presence of Dean-type vortices, and impingement effects due to fluid inertia. As the

fluid reaches the fourth passage, it is apparent that there are two distinct fluid streams along the inner and outer walls. These streams combine and then dissipate upon reaching the outlet at the end of the fourth passage. These results are consistent with those found in previous papers exploring this geometry and similar configurations [1].

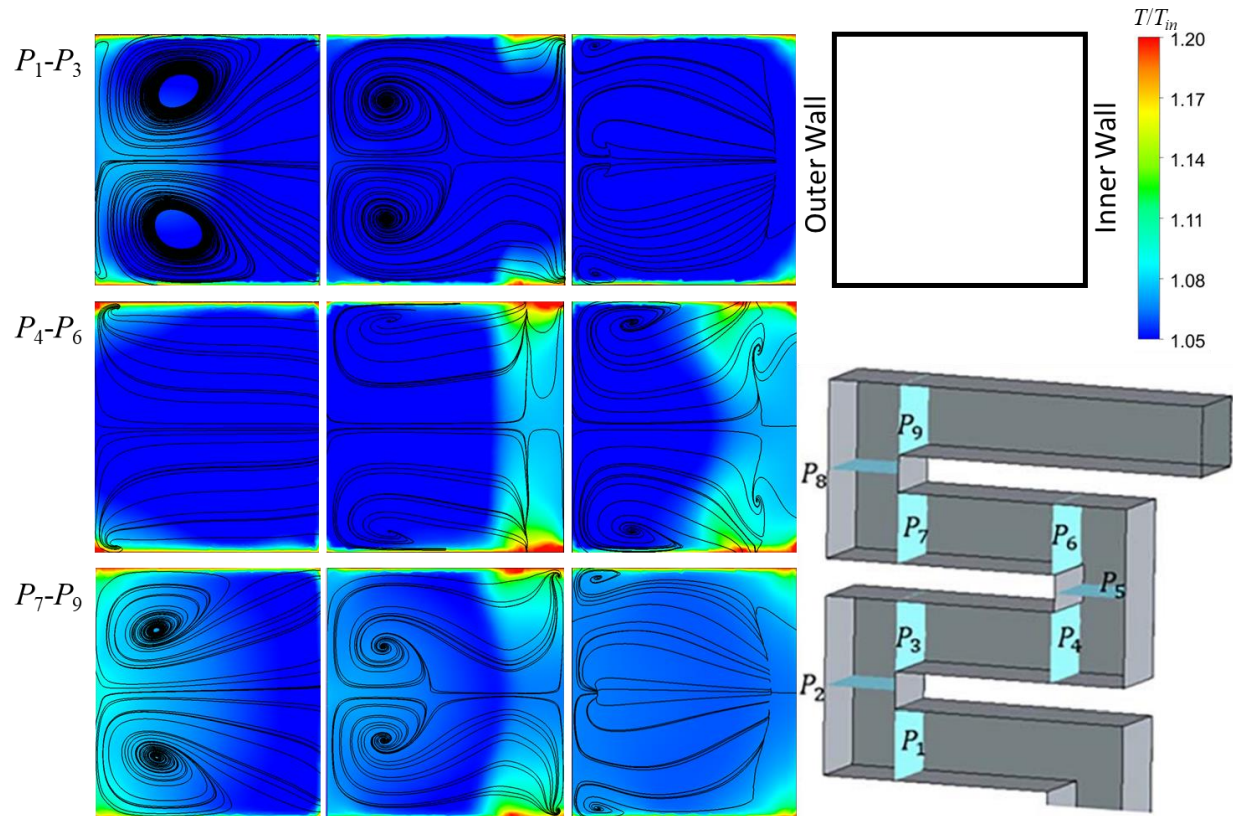


Figure 2.2: Smooth channel velocity vector flow fields with normalized fluid temperature contour at planes orthogonal to bulk coolant flow (under stationary conditions, $Re = 18933$, $Ro = 0$).

Smooth Channel Configuration Under Rotating Conditions

The added element of rotation to the system introduces Coriolis force acting on the coolant flowing throughout the channel, resulting in nonuniform heat transfer between the

leading and trailing sides. While the serpentine passages of the configurations were designed to negate the effect of these forces, the radially outward inlet passage still experienced Coriolis effects. As such, the trailing side of the inlet passage had a higher heat transfer than that of the stationary case, while the leading side featured a lower heat transfer than that of the stationary case. This attributed to the first passage on the trailing side having a much larger amount of heat transfer than its leading counterpart. As the fluid continued through the remaining passages, the Coriolis effects were primarily cancelled out, resulting in similar heat transfer levels between the leading and trailing sides. This can be seen in Figure 2.3, where the velocity flow fields closest to the inlet display a contour skewed towards the trailing side. These contours then become much more even between the leading and trailing sides as the flow progresses through the channel.

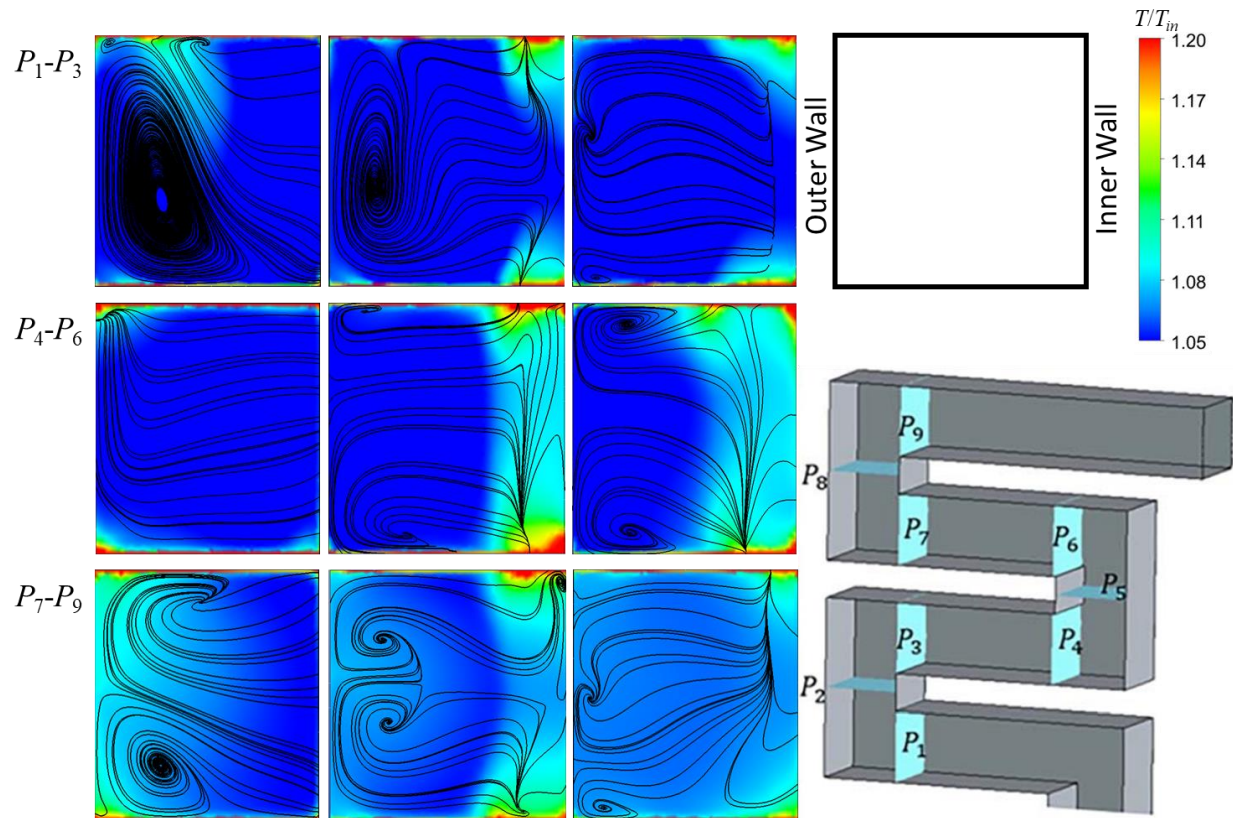


Figure 2.3: Smooth channel velocity vector flow fields with normalized fluid temperature contour at planes orthogonal to bulk coolant flow (under rotating conditions, $Re = 18933$, $Ro = 0.11$).

Compared to the stationary case, the rotating case was observed to have a very minor enhancement in heat transfer due to the additional effects of the Coriolis force acting on the fluid. Overall, the differences in heat transfer enhancement were only impactful in the first passage.

V-Ribbed Channel Configuration Under Stationary Conditions

Figure 2.4 shows the normalized Nusselt number contours at the wall under both stationary and rotating conditions for the V-Ribbed channel configuration. The fluid enters the

first passage in a similar manner to the smooth channel configuration, and either impinges on the inner horizontal wall or follows the outer horizontal wall due to a low pressure gradient, generating increased heat transfer enhancement at both locations. The heat transfer throughout the entire channel is elevated due to the generation of secondary flows by the V-Ribbed turbulators along both the inner and outer walls.

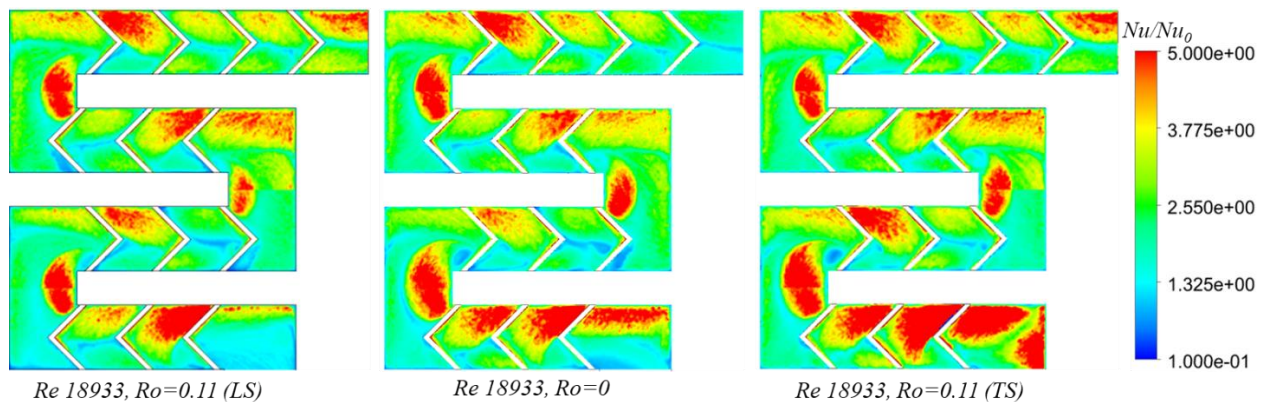


Figure 2.4: Detailed Nusselt number ratio contour for the V-Ribbed channel configuration under stationary and rotating conditions.

Like the Smooth channel configuration, the first passage experienced enhanced heat transfer due to the impingement of coolant directly onto the inner horizontal wall upon exiting the inlet passage. It was observed that the 180 degree bends featured elevated higher heat transfer levels than the rest of the passage. This is a result of the combination of rib-induced secondary flows and the curvature-induced radial pressure gradient, which enabled the formation of multiple Dean-type vortices in the bend regions. The presence of two separate pairs of Dean-type vortices can be observed at several points in Figure 2.5. Due to the presence of the V-Ribbed turbulators, the overall Nusselt number ratio seen in this configuration was greater than that of the smooth channel configuration, indicating a higher level of heat transfer enhancement.

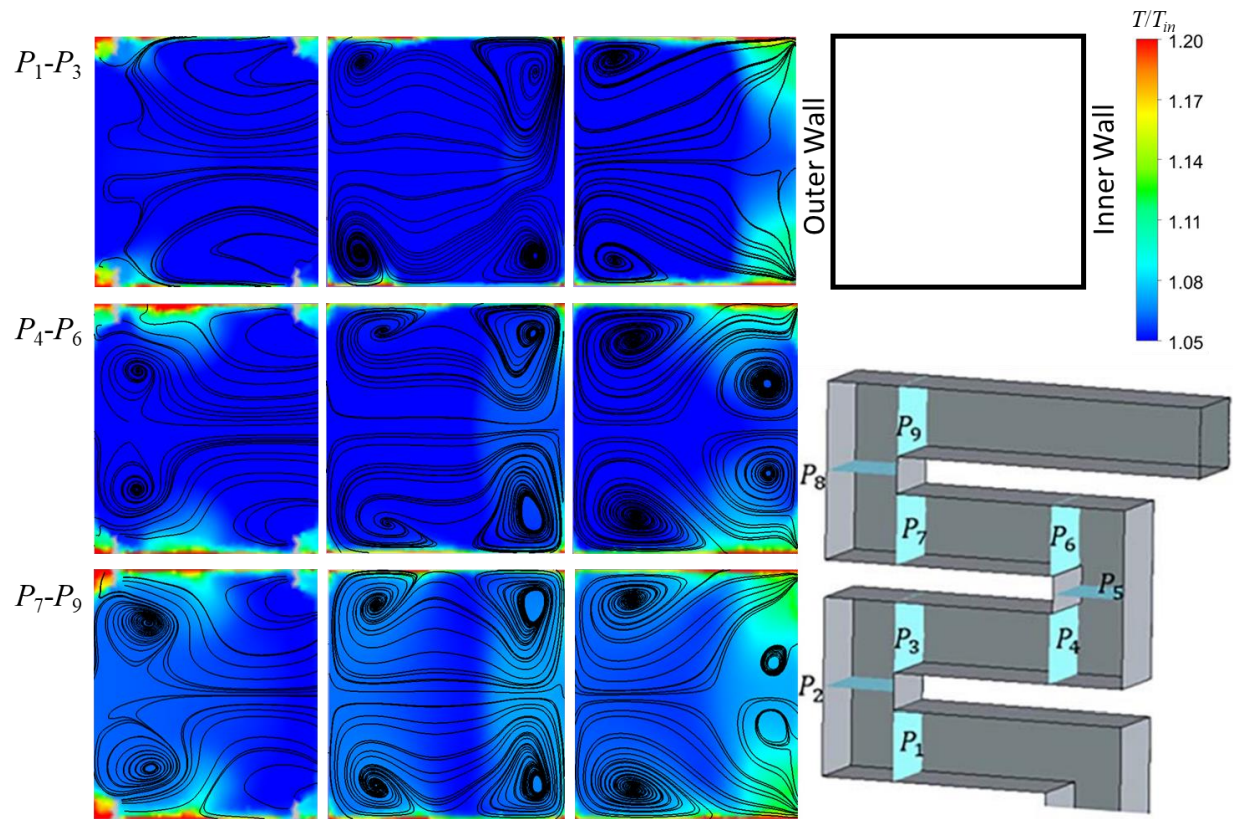


Figure 2.5: V-Ribbed channel velocity vector flow fields with normalized fluid temperature contour at planes orthogonal to bulk coolant flow (under stationary conditions, $Re = 18933$, $Ro = 0$).

V-Ribbed Channel Configuration Under Rotating Conditions

The rotating V-Ribbed channel configuration featured slightly higher overall heat transfer levels than its stationary counterpart, leading to a higher average Nusselt number ratio in each passage. Due to the combination of inlet conditions and Coriolis effect, the first passage produced similar results as in the rotating smooth configuration, where the trailing side experienced a higher heat transfer when compared to the stationary V-Ribbed case, and the leading side experienced a lower heat transfer. The leading side featured two distinct fluid flows,

resulting in a reduced effectiveness of the V-Rib turbulators. On the trailing side however, most of the fluid was pushed towards the outside edge, leading to an increase in rib effectiveness.

These conditions were still present, to a much lesser degree, in the second passage.

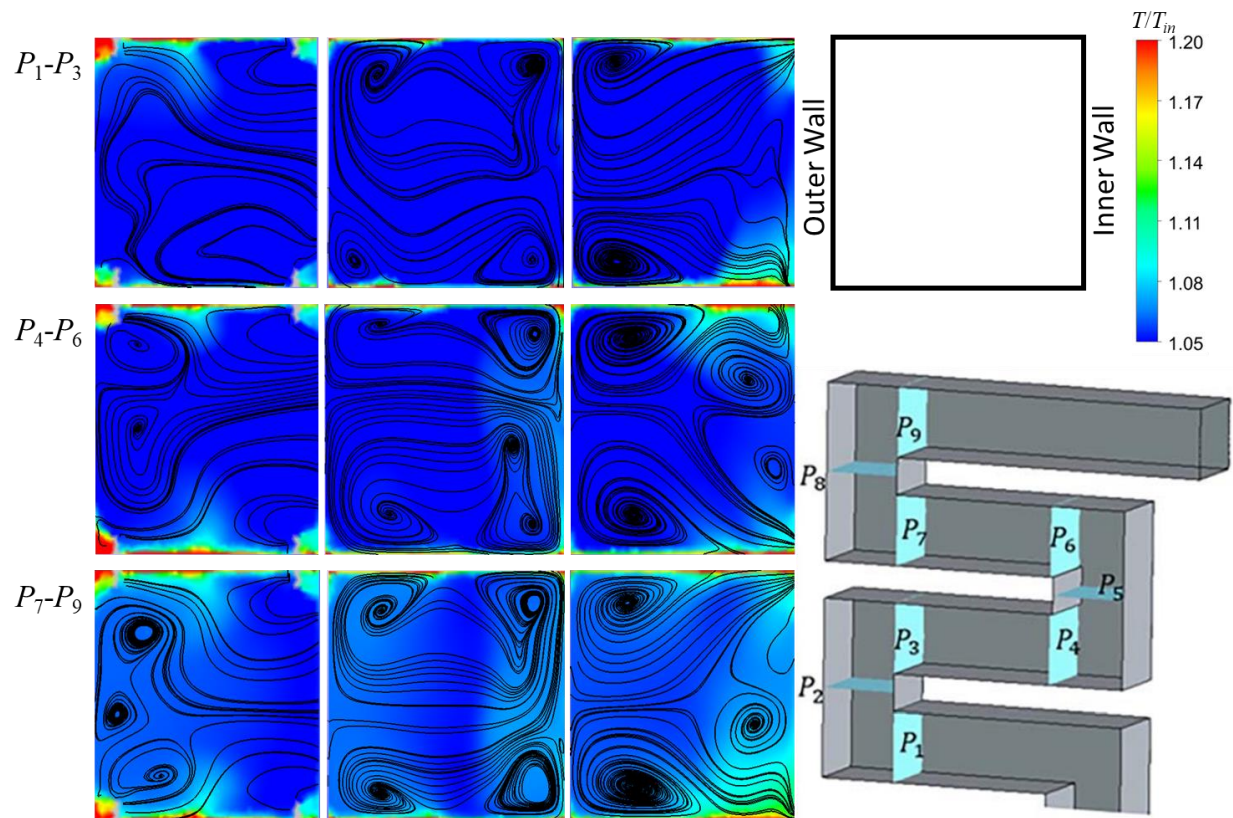


Figure 2.6: V-Ribbed channel velocity vector flow fields with normalized fluid temperature contour at planes orthogonal to bulk coolant flow (under rotating conditions, $Re = 18933$, $Ro = 0.11$).

As the fluid entered the third and fourth passages, the heat transfer levels between the leading and trailing sides normalized due to the effect of the serpentine geometry on the Coriolis effect. After the effects of the inlet conditions were essentially negated, the subsequent passages

featured only a slightly elevated level of heat transfer when compared to the stationary case. This level of heat transfer was observed to increase as the flow progressed through the final passages.

Broken V-Ribbed Channel Configuration Under Stationary Conditions

The Broken V-Ribbed channel configuration yielded slightly higher overall heat transfer levels than the V-Ribbed channel configuration due to the nature of the geometry. The gap in the middle of the ribs allowed for less turbulent mixing in the horizontal segments, as more fluid could circumvent the secondary flows induced by the ribs. While this resulted in reduced heat transfer in the horizontal segments, it allowed for elevated levels of heat transfer enhancement in the 180 degree bends. Figure 2.7 shows the normalized Nusselt number contours at the wall for the stationary and rotating cases.

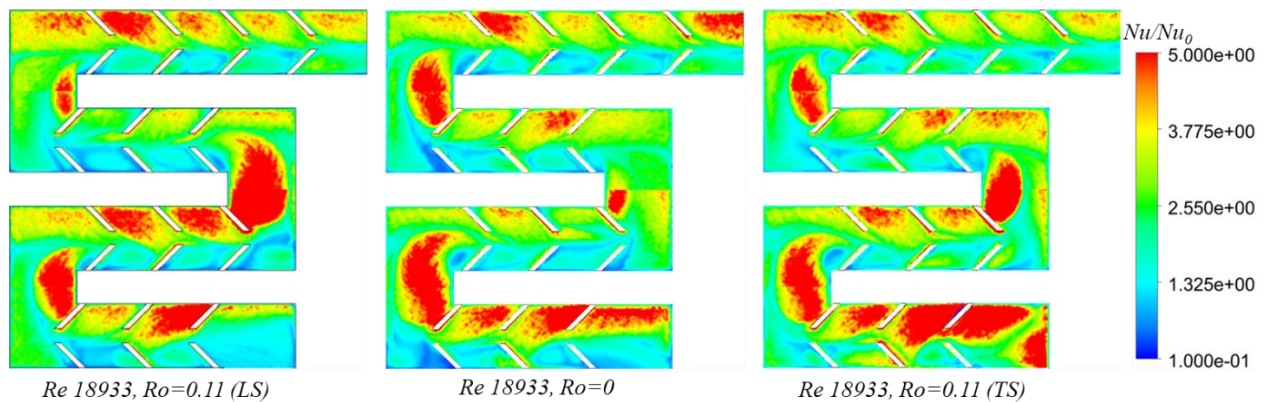


Figure 2.7: Detailed Nusselt number ratio contour for the Broken V-Ribbed channel configuration under stationary and rotating conditions.

As experienced in the previous configurations, the inlet conditions played a large part in the elevated heat transfer levels in the first passage. After entering the first passage, the flow

either impinged upon the inner horizontal wall, continued along the passage through the gap in the ribs, or were wrapped up in the rib-induced secondary flows.

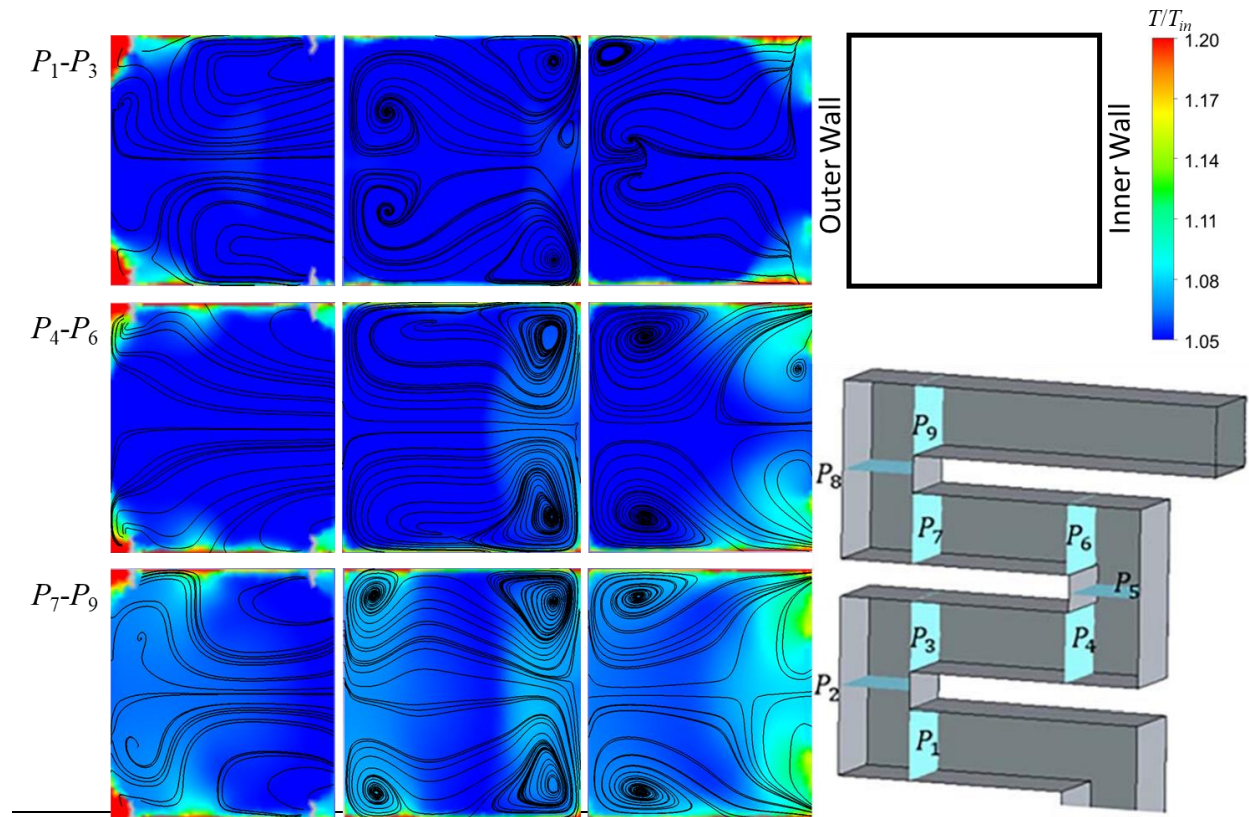


Figure 2.8: Broken V-Ribbed channel velocity vector flow fields with normalized fluid temperature contour at planes orthogonal to bulk coolant flow (under stationary conditions, $Re = 18933$, $Ro = 0$).

Broken V-Ribbed Channel Configuration Under Rotating Conditions

Just as with the previous rotating configurations, the first passage was still influenced by the Coriolis force. This manifested itself in the much higher heat transfer levels in the trailing side and much lower heat transfer levels in the leading side. The effect of the Coriolis force remained a factor after the first passage, leading to a marginally increased level of heat transfer

in each passage when compared to the stationary configuration of the same geometry. Dean-type vortices were still observed in the orthogonal plane, as seen in Figure 2.9, but were also skewed towards the trailing side, as expected.

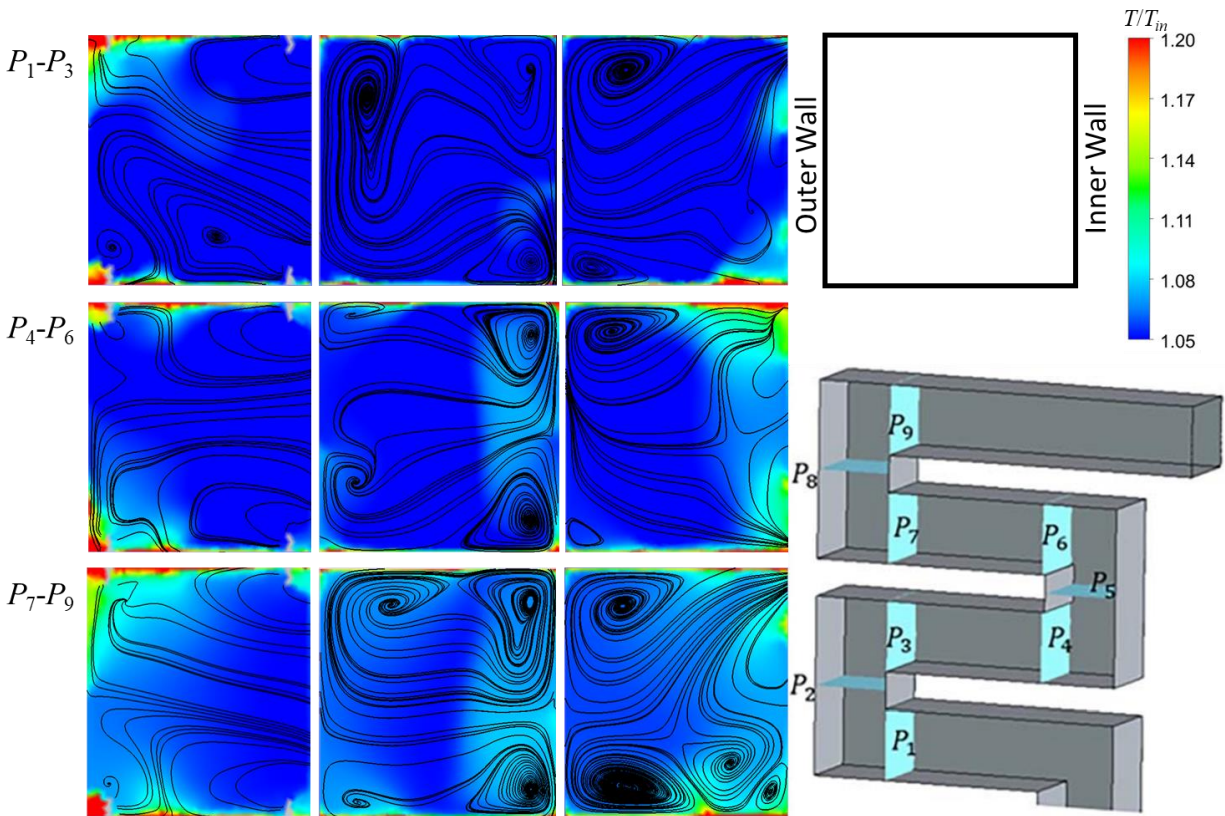


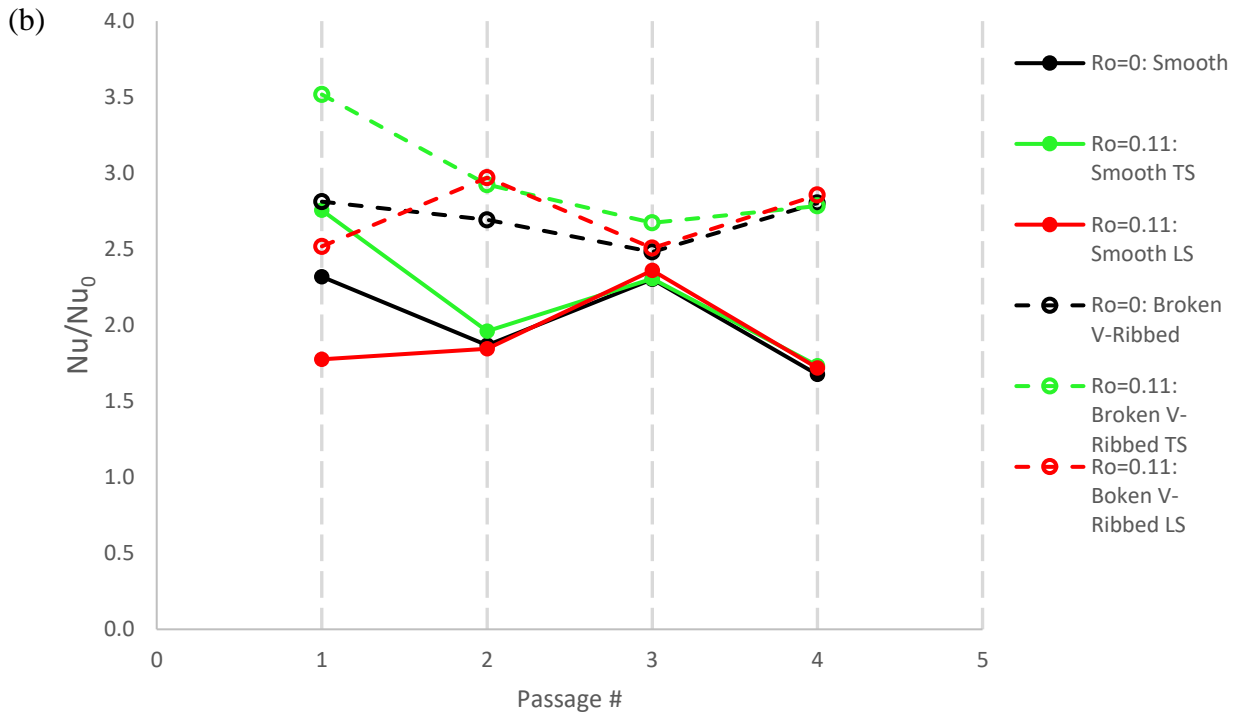
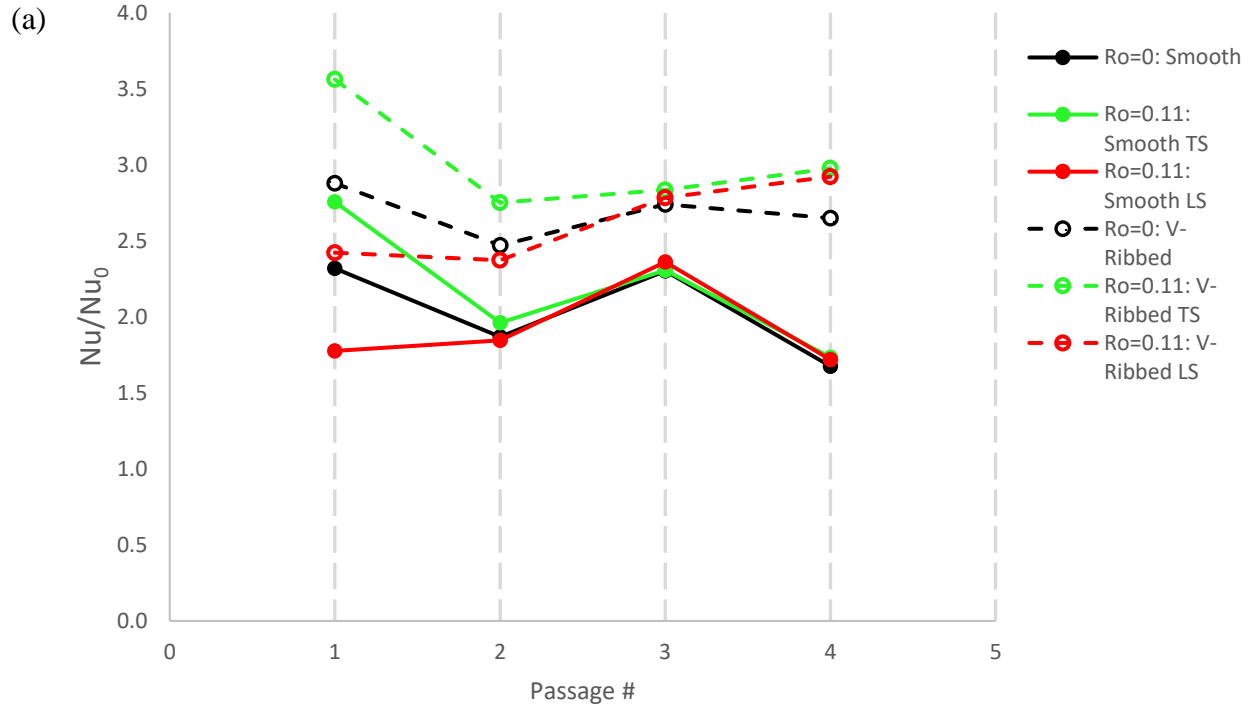
Figure 2.9: Broken V-Ribbed channel velocity vector flow fields with normalized fluid temperature contour at planes orthogonal to bulk coolant flow (under rotating conditions, $Re = 18933$, $Ro = 0.11$).

Passagewise-Averaged Nusselt Number Ratio Under Stationary and Rotating Conditions

Figure 2.10 shows the passagewise-averaged Nusselt number ratios for the Smooth channel, V-Ribbed channel, and Broken V-Ribbed channel cases. As previously discussed, the Coriolis effect acting upon the inlet conditions attributed to the discrepancy between the leading

and trailing sides in the first passage, as well as the second passage to an extent. Apart from both first passage leading sides, the two configurations containing heat transfer enhancement features were observed to have had substantially higher passagewise-averaged Nusselt number ratios than the unmodified Smooth channel configuration. In both the stationary and rotating cases, the Broken V-Ribbed configuration narrowly outperformed the V-Ribbed configuration in terms of overall Nusselt number ratio, corresponding to a higher heat transfer enhancement.

Figure 2.10: Passagewise-averaged Nusselt number ratio under stationary and rotating conditions for (a) V-Ribbed and Smooth channel configurations and (b) Broken V-Ribbed and Smooth channel configurations.



Friction Factor, Overall Nusselt Number Ratio, and Thermal Hydraulic Performance

Static pressure measurements were taken to determine the frictional losses due to the bends in the channel. As expected, the static pressure was observed to decrease over the course of the channel. While the serpentine design was implemented to reduce the impact of Coriolis effects, it also had the added effect of increasing the required pumping power to propel the coolant at the given mass flow rate. The normalized friction factor was determined from the following equation:

$$\frac{f}{f_0} = \frac{\Delta p}{2\rho V^2} \frac{d_h}{L_{total}} \frac{1}{0.046 \text{Re}^{-0.2}} \quad (2.1)$$

The friction factor, as well as the pumping power required are shown in Figure 2.11. The equation for pumping power is displayed below:

$$\text{Pumping Power, } P = \dot{V} \Delta_{total} \quad (2.2)$$

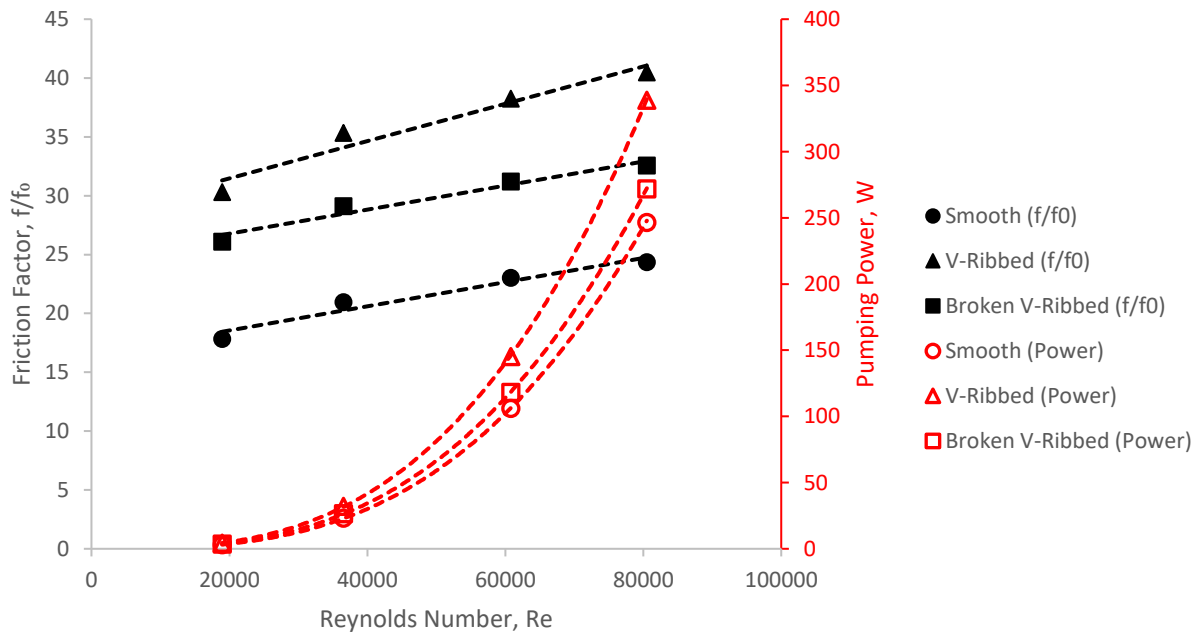


Figure 2.11: Normalized friction factor and pumping power variation with Reynolds number.

Figure 2.11 also shows how the bends of the serpentine geometry contributed to the frictional losses throughout the channel. The presence of ribbed turbulators also added to the overall frictional losses. Since the Broken V-Ribbed configuration featured a gap in its ribs, the friction factor was noticeably lower than that of the V-Ribbed configuration. As expected, the pumping power was shown to increase monotonically with the Reynolds number. All friction factor and pumping power values were obtained under stationary conditions.

The globally averaged gain in heat transfer is shown in Figure 2.12. For all configurations, the Nusselt number ratio was observed to decrease as the Reynolds number increased, which is a trend found in previous similar studies of this nature [3]. The globally averaged Nusselt number ratio and thermal hydraulic performance were obtained for all stationary cases at four Reynolds numbers. The globally averaged Nusselt number ratios were also obtained for the rotating cases at a single Reynolds number. In the observed rotating cases, the elevated heat transfer levels in the trailing side were attributed to the effect of the Coriolis force on the inlet flow. As such, the difference in heat transfer enhancement between the leading and trailing sides was primarily found in the first passage, with some remnants of the effects of Coriolis force in the second passage. The thermal hydraulic performance, or THP, was calculated using the equation below:

$$THP = \frac{Nu/Nu_0}{(f/f_0)^{1/3}} \quad (2.3)$$

The thermal hydraulic performance was shown to decrease with increasing Reynolds numbers. At the lowest Reynolds number tested, the Broken V-Ribbed configuration had the highest THP, but the differences between the THPs of the configurations decreased as the Reynolds number increased.

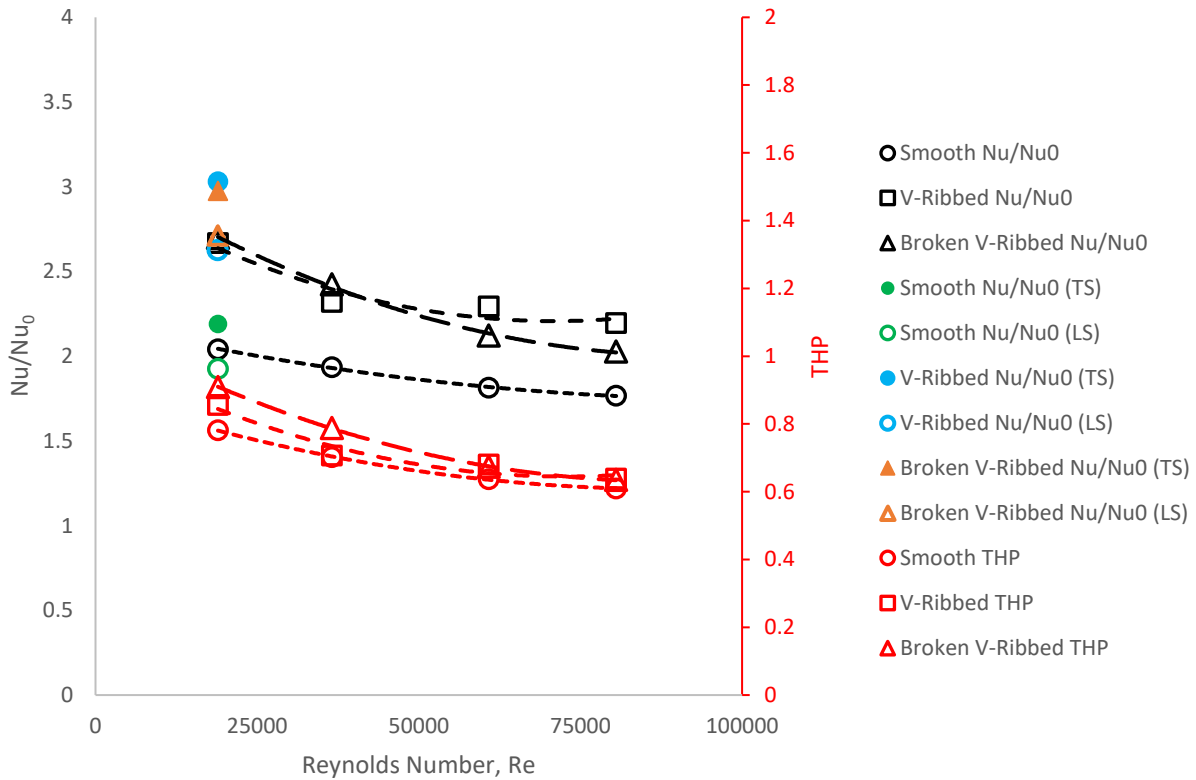


Figure 2.12: Globally averaged Nusselt number ratio (Nu/Nu_0) and thermal hydraulic performance variation with Reynolds number.

Conclusion

This study explores two novel heat transfer enhancement features to a four-passage serpentine cooling design to improve upon the existing design. Numerical simulations were performed under stationary and rotating conditions using ANSYS Fluent. The THP values recorded in both the V-Ribbed and Broken V-Ribbed were higher than those recorded in the Smooth channel configuration, with the overall Nusselt number ratios of the two introduced designs being noticeably higher. The two configurations proposed in this study were both clear improvements over the Smooth channel design, with the Broken V-Ribbed configuration being the superior of the two due to its higher THP value.

REFERENCES

- [1] Singh, P., Ji, Y., and Ekkad, S. V. (February 14, 2019). "Multi-Pass Serpentine Cooling Designs for Negating Coriolis Force Effect on Heat Transfer: Smooth Channels." *ASME. J. Turbomach.* July 2019; 141(7): 071001.
- [2] J.C. Han, Y.M. Zhang, High performance heat transfer ducts with parallel broken and V-shaped broken ribs, *International Journal of Heat and Mass Transfer*, Volume 35, Issue 2, 1992, pp. 513-523.
- [3] Singh, P., Ji, Y., and Ekkad, S. V. (February 15, 2019). "Multipass Serpentine Cooling Designs for Negating Coriolis Force Effect on Heat Transfer: 45-deg Angled Rib Turbulated Channels." *ASME. J. Turbomach.* July 2019; 141(7): 071003.
- [4] Singh, P., Sarja, A., and Ekkad, S. V. (August 11, 2020). "Experimental and Numerical Study of Chord-Wise Eight-Passage Serpentine Cooling Design for Eliminating the Coriolis Force Adverse Effect on Heat Transfer." *ASME. J. Thermal Sci. Eng. Appl.* February 2021; 13(1): 011026.
- [5] Sarja, A, Madhavan, S, Singh, P, & Ekkad, SV. "Effect of Blade Profile on Four-Passage Serpentine Configuration Designed to Negate Coriolis Effect on Heat and Fluid Flow." *Proceedings of the ASME Turbo Expo 2019: Turbomachinery Technical Conference and Exposition. Volume 5A: Heat Transfer.* Phoenix, Arizona, USA. June 17–21, 2019. V05AT11A012. ASME.
- [6] Lamont, J. A., Ekkad, S. V., and Alvin, M. A. (February 24, 2012). "Detailed Heat Transfer Measurements Inside Rotating Ribbed Channels Using the Transient Liquid Crystal Technique." *ASME. J. Thermal Sci. Eng. Appl.* March 2012; 4(1): 011002.